Gravity-wave influences on Arctic mesospheric clouds as determined by a Rayleigh lidar at Sondrestrom, Greenland

Jeffrey P. Thayer,[1] Markus Rapp,[2] Andrew J. Gerrard,[3] Eggert Gudmundsson,[4] and Timothy J. Kane[5]

Received 25 March 2002; accepted 29 January 2003; published 26 March 2003.

[1] Since 1994, Rayleigh lidar measurements of the Arctic middle atmosphere have been conducted at the Sondrestrom research facility near Kangerlussuaq, Greenland (67.0N,50.9W). The summer lidar observations typically cover the late June through August period. From these observations, 220 hours of noctilucent clouds (NLCs) have been detected by the lidar spanning 16 hours of local time. Organizing the cloud characteristics irrespective of local time reveals the most common cloud height as 82.5 km, the most common full-width-half-maximum (FWHM) as 0.7 km, and the most common peak volume backscatter coefficient as 20.0×10^{-11} $m^{-1}sr^{-1}$. The FWHM is noticeably thinner than determined by other lidar observations of NLCs in Norway and the South Pole. We found the mean backscatter strength to increase and the FWHM to decrease with decreasing cloud height. In addition, the cloud slopes with time are greater for the thicker weaker clouds at higher altitudes than the thinner stronger clouds at lower altitudes. Gravity-wave signatures are routinely observed in the cloud detections. Upon estimating stratospheric wave activity in the data, we observed stronger cloud backscatter during low gravity-wave activity and weak cloud backscatter during high gravity-wave activity. To help support these results, simulations from a microphysical cloud model were performed under summer mesospheric conditions with and without gravity-wave activity. Upon including short-period ($\sim$2–3 hours) gravity-wave activity, the model simulation reproduced the behavior observed in the ensemble cloud properties by producing a broader altitude distribution, weaker backscatter strength, and thinner clouds. *INDEX TERMS:* 0305 Atmospheric Composition and Structure: Aerosols and particles (0345, 4801); 0320 Atmospheric Composition and Structure: Cloud physics and chemistry; 0340 Atmospheric Composition and Structure: Middle atmosphere—composition and chemistry; 0669 Electromagnetics: Scattering and diffraction; 1655 Global Change: Water cycles (1836); *KEYWORDS:* noctilucent clouds, gravity waves, Rayleigh lidar, volume backscatter coefficient, polar mesosphere

Citation: Thayer, J. P., M. Rapp, A. J. Gerrard, E. Gudmundsson, and T. J. Kane, Gravity-wave influences on Arctic mesospheric clouds as determined by a Rayleigh lidar at Sondrestrom, Greenland, *J. Geophys. Res.*, *108*(D8), 8449, doi:10.1029/2002JD002363, 2003.

1. Introduction

[2] A direct manifestation of the dynamically driven cold summer polar mesosphere is the formation of noctilucent clouds (NLCs), consisting for the most part of ice. Polar mesospheric clouds are the space-observed equivalent of NLCs and, given their more recent excursions to middle latitudes, the nomenclature for these clouds could be reduced to simply mesospheric clouds. However, since the reported observations in this paper are from an Arctic ground-based site, we will use the term NLC to describe our detections. NLC formation is initiated by water vapor condensing on preexisting condensation nuclei (either dust particles or large cluster ions) at very low pressures that exist in and around the cold summer mesopause [e.g., *Thomas*, 1991; *Hervig et al.*, 2001]. Over most of the lifetime of the ice particles, the water vapor pressure will be much larger than the saturation vapor pressure over ice (i.e., supersaturation), resulting in a continued growth rate and subsequent sedimentation. Because the saturated vapor pressure over ice depends exponentially on temperature, the falling particle will transition out of the supersaturated region and begin to lose size rapidly as it sublimates.

[3] This description is the basic growth-sedimentation-sublimation model described early on, for example, by *Hesstvedt* [1961, 1962], *Charlson* [1965], and *Reid* [1975].

[1]SRI International, Menlo Park, California, USA.
[2]Leibniz Institute of Atmospheric Physics, Kühlungsborn, Germany.
[3]College of Agriculture and Technology at Morrisville, State University of New York, Morrisville, New York, USA.
[4]Danish Meteorological Institute, Observation Department, Copenhagen, Denmark.
[5]The Pennsylvania State University, College Park, Pennsylvania, USA.

Copyright 2003 by the American Geophysical Union.
0148-0227/03/2002JD002363$09.00

A more comprehensive modeling study was introduced by *Turco et al.* [1982] accounting for many of the physical processes expected to be important. This model has evolved over time with *Jensen and Thomas* [1988, 1994], *Jensen et al.* [1989], and, most recently, *Rapp et al.* [2002].

[4] The pervasiveness of wave activity, particularly tidal and gravity waves, in the mesopause region led to multidimensional model simulations to investigate the impact of waves on NLC formation, characteristics, and behavior. The work of *Jensen et al.* [1989] introduced diurnal variations on temperature and vertical wind using tidal models and incorporated eddy diffusion variations caused by gravity-wave breaking. They found these tidal perturbations produced significant local time variability in model cloud brightness and cloud height, with maximum brightness and minimum height occurring near local midnight. Gravity-wave influences were introduced to the model by *Jensen and Thomas* [1994]. Short-period gravity waves of less than a few hours induced temperature perturbations that decreased the model cloud brightness. They postulated that the mesopause temperature must be about 5 K colder for NLCs to form when gravity waves are present than when they are not present. *Rapp et al.* [2002] reanalyzed ionization gauge measurements from seven sounding rocket experiments and derived temperatures between 70 and 110 km at 200 m resolution. They found significant temperature fluctuations between 82 and 95 km exceeding 5 K, and, in three of the seven experiments, provided observational evidence of NLC occurrence in local temperature minima, presumably induced by gravity-wave perturbations. They also performed numerical simulations of NLC generation in the presence of gravity waves that demonstrate a complex interplay among sedimentation, vertical advection, and simultaneous growth.

[5] Recently, *Klostermeyer* [1998] described a separate model scenario where a mean upward velocity, necessary to maintain the cold summer mesopause temperatures, compensates for particle sedimentation enabling particle growth and evaporation to occur at various altitudes essentially controlled by tide/wave associated motions and, consequently, independent of particle size. *Klostermeyer* [1998] suggests that the timescale for particle growth can be much faster if vertical motions resulting from tides or gravity waves are considered. *Charlson* [1965] also suggested an upward wind speed to help keep the microscopic particles within the supersaturation region long enough so that they may grow to visible sizes.

[6] *Klostermeyer* [2001] introduced tidal temperature variability into his NLC model to account for the expected day-to-day variability in tidal-induced mesospheric temperatures, whose impact on NLC formation is significant because of their nonlinear response to temperature changes. *Klostermeyer* [2001] demonstrated that the temperature variations improved the ability of the model to reproduce the strong semidiurnal variations in NLC height and backscatter strength observed at the ALOMAR lidar station in northern Norway.

[7] Lidar observations provide a unique measurement of basic NLC properties, specifically cloud height, cloud width, and backscatter strength, with good local time coverage that can complement the satellite observations, and test the theories and models of microphysical cloud formation. The results of *von Zahn et al.* [1998] using a large data set of NLC detections from the ALOMAR lidar facility in northern Norway indicate diurnal and semidiurnal tidal influences have a dominant impact on the NLC behavior with local time. Also, recent observations of NLCs from the South Pole station by *Chu et al.* [2001b] observe diurnal and semidiurnal tidal influences with local time, although the basic properties of the NLCs, such as height and correlation with backscatter strength, seem to differ from those observed in northern latitudes.

[8] In this paper, we analyze a large data set of NLC detections by a Rayleigh lidar located in Sondrestrom, Greenland, whose many observations indicate a strong presence of gravity waves. The presence of gravity waves will act to perturb the basic state of the mesopause region and consequently affect the microphysics responsible in forming the cloud. The lidar-derived characteristics of these clouds represent the outcome of this influence. Assuming the gravity-wave activity to be a random, stochastic process, the ensemble of NLC detections will demonstrate the distribution of noctilucent cloud height, backscatter strength, and thickness resulting from a gravity-wave dominated environment.

[9] In the following sections, the Sondrestrom, Greenland, lidar observations, consisting of 220 hours of NLC detections, will be analyzed and the strong influence of gravity waves will be demonstrated. The individual NLC detections will then be fitted to produce the basic properties of cloud height, width, and backscatter strength. These cloud properties are then collected to evaluate their behavior with local time. Further, as the gravity-wave influences are rather random, the data are organized irrespective of local time to demonstrate the collective behavior of the basic cloud properties. We then incorporate model runs from the Community Aerosol and Radiation Model for Atmospheres (CARMA) model [*Rapp et al.*, 2002], to investigate the influence of gravity waves on the cloud properties and their basic characteristics. The purpose of the model run is not to compare directly with the observed lidar cloud parameters, but to demonstrate there is a principal physical cause (i.e., gravity waves) that acts to modify the cloud parameters in a specific way.

2. NLC Detectability by Lidar

[10] The detectability of an NLC by lidar is primarily dictated by the volumetric backscatter properties of the aerosols making up the cloud and the performance capabilities of the lidar system, particularly during polar summer observations. Independent of its growth path, an NLC particle must grow to a radius in excess of about 20 nm in order to be detected by present-day lidar systems operating at visible wavelengths [*von Cossart et al.*, 1999]. This limiting radius is because the backscattered lidar signal has a dependence on the particle radius to approximately the sixth power. Thus lidars are essentially observing NLCs that have existed for many hours to days as they go through a number of evaporation and growth cycles before being detected. Moreover, lidars are observing the larger radii of the particle size distribution making up the cloud, and this must be kept in mind when comparing the lidar-derived NLC properties with other observing techniques.

[11] It is often convenient to analyze the presence of NLCs, or aerosols in general, in the elastic backscatter lidar signal by using the ratio of total backscatter coefficient to molecular backscatter coefficient, that is, the lidar backscatter ratio. A ratio exceeding unity indicates aerosol scattering is present in the signal. The aerosol volume backscatter coefficient, $\beta_\pi^A(\lambda, z)$, is the product of the cloud number density and the differential backscatter cross section integrated over all radii. The aerosol differential backscatter cross section can be shown to be approximately proportional to the radius raised to the sixth power. As discussed by *Thayer et al.* [1995], for backscatter ratios significantly exceeding 1.0 (typical for NLCs), the volume backscatter coefficient (VBC) can be determined more accurately from the lidar signal than the backscatter ratio, as the relative error for $\beta_\pi^A(\lambda, z)$ does not depend on the background molecular number density at the height of the cloud. The lidar-derived expression for the aerosol VBC can then be approximated (assuming no aerosols are present at the normalization altitude and no extinction of the signal occurs between the normalization altitude and the cloud) as

$$\beta_\pi^A(\lambda, z) = \frac{S(\lambda, z) n(z^*)}{S(\lambda, z^*)} \sigma_\pi^M(\lambda), \tag{1}$$

where z^* is the normalization altitude void of any aerosol signal contamination (usually taken to be 30 km), $S(\lambda,z)$ and $S(\lambda, z^*)$ are the noise-subtracted, range-corrected lidar signal at z and z^* altitudes, respectively, $n(z^*)$ is the atmospheric number density at z^*, and $\sigma_\pi^M(\lambda)$ is the molecular backscatter cross section. As the normalized lidar signal (after noise subtraction and range correction) is equal to the relative atmospheric density, then the aerosol backscatter coefficient at the cloud height z_A is directly related to the molecular backscatter coefficient at some altitude z_M, such that

$$\beta_\pi^A(\lambda, z_A) = n^A(z_A)\sigma_\pi^A(\lambda, r) = \beta_\pi^M(\lambda, z_M) = n(z_M)\sigma_\pi^M(\lambda), \tag{2}$$

where $n^A(z_A)$ is the number density of NLC particles present at the NLC altitude z_A, and $\sigma_\pi^A(\lambda, r)$ is the aerosol backscatter cross section. This leads to the often referred to Rayleigh equivalent altitude of NLC detections [e.g., *Hansen et al.*, 1989], where the signal strength of the cloud equates to the altitude with equivalent signal strength from molecular scatter. This relationship is useful for evaluating whether the lidar system is capable of detecting molecular VBCs within the range of the expected NLC volume backscatter coefficient. In this way, it can be determined whether for a given lidar performance the lidar should be expected to detect an NLC and of what magnitude.

[12] Typically, scattering of a lidar signal operating at 532 nm by NLC aerosols produce backscatter signals that are equivalent to molecular or Rayleigh scattered signals that occur over the range from 45 to 70 km or more in altitude [*Thayer et al.*, 1995]. This altitude range in signal relates to a possible range of aerosol VBCs of 200×10^{-11} $m^{-1}sr^{-1}$ at 45 km to 4×10^{-11} $m^{-1}sr^{-1}$ at 70 km, assuming a constant scale height of 6.2 km. If the cloud number density is assumed not to change significantly, then this factor of 50 change in aerosol backscatter coefficient relates to a radius change of only a factor of 1.9, illustrating the lidar is observing only a small part of the particle size distribution. It will be shown that the most common NLCs detected by our system are around 20×10^{-11} $m^{-1}sr^{-1}$ (or an equivalent Rayleigh altitude of about 60 km). Thus lidar systems must be capable of measuring the noise-subtracted, range-corrected Rayleigh signal accurately above 60 km in order to detect the more common moderate to weak NLCs. The time-varying levels of the solar background during Arctic summer observations make this threshold a challenge for certain local times and certain parts of the summer season. Thus the fact that a lidar does not observe an NLC may be as much a threshold detection problem as a physical condition of the upper mesospheric region.

3. Observations

[13] A description of the Arctic Lidar Technology (ARCLITE) facility at the Sondrestrom research site in Greenland is provided by *Thayer et al.* [1997] and our summertime operations are described by *Thayer et al.* [1996]. A reduction in our system's telescope field of view to 0.2 mrad in 1999 improved our local time and seasonal coverage of NLCs by increasing the signal-to-noise by a factor of four.

[14] From the Sondrestrom lidar data set, we have analyzed all data taken from 1994 through 2000 for the months of late June through August. From this data set we have determined the local time distribution of all lidar observations with and without NLC detections and our sensitivity threshold in detecting an NLC. These results are presented in Figure 1. The local time distribution for all lidar observations during the NLC season are presented in Figure 1a with each observation referring to a 10-min data record. The total number of operating hours is over 900. Here it can be seen that the majority of observations occurred within the local times between 20 local solar time (LST) and 04 LST with limited observations in the midday local time sector, provided by the 1999 and 2000 data sets. The distribution of observations is peaked at local midnight with nearly an equal partition of observations on either side of midnight.

[15] Included in Figure 1a is the subset of observations where an NLC was clearly detected by the lidar. The distribution is similar to the total number of observations with a detection occurring about 20% of the time. Thus far, the lidar has observed NLCs covering 16 hours of local time between 18 and 10 LST. The greatest concentration of cloud detections occur in and around local midnight, largely because the background signal is at its lowest during this time, thus providing the highest sensitivity for detection by the lidar.

[16] Figure 1b is a scatterplot of the VBC evaluated when signal errors reach 10%. The data have been integrated for 10 min at 384 m vertical resolution (actual data taking integrations were 1 min and typically 48 or 192 m throughout the seven years). The approach used was to determine from a 10-min, noise-subtracted lidar signal profile the altitude by which the signal error reached 10%. Using Poisson statistics, that level would be equivalent to a signal of 100 counts per 10 min per 384 m bins. The determined

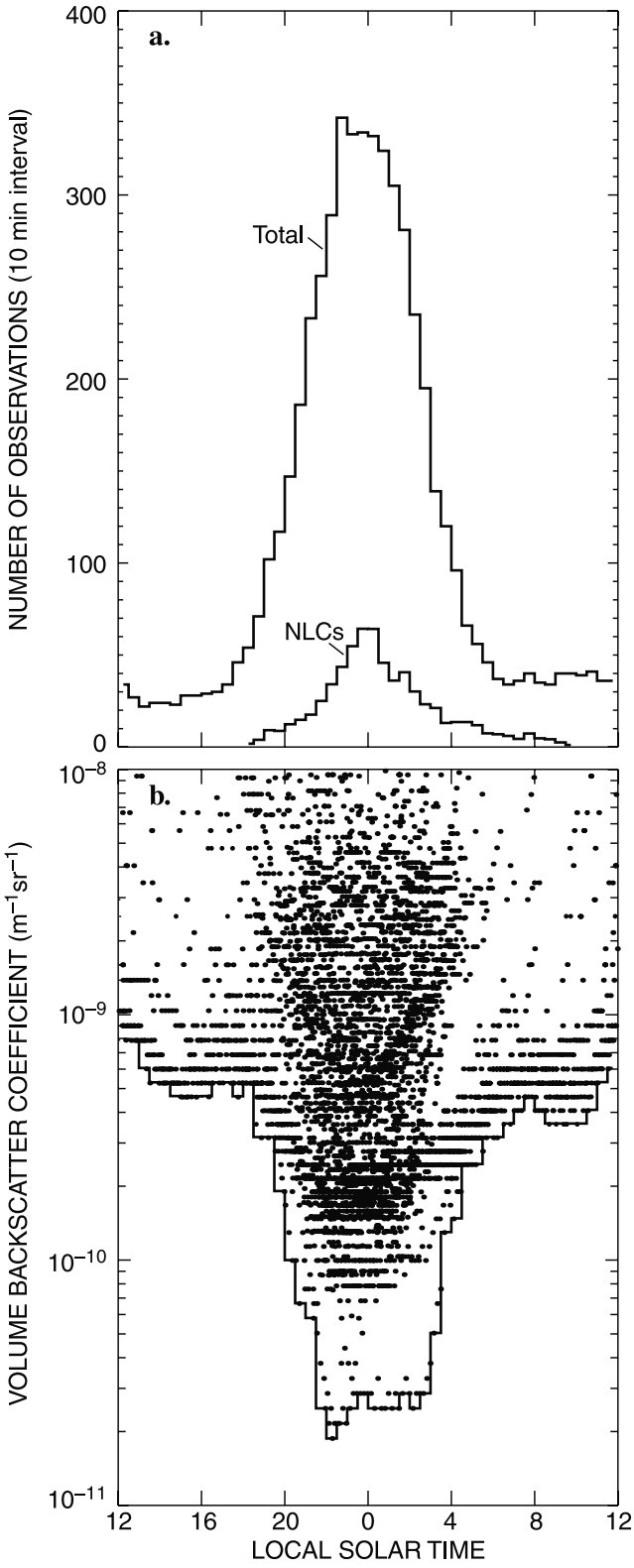

Figure 1. (a) Distribution of total lidar observations from 1994–2000, covering the months of June, July, and August, and NLC detections at 10-min intervals. (b) All VBC values from every 10-min data record taken for the months of June, July, and August from 1994–2000 organized in 30-min local time bins.

altitude was then used to estimate the VBC from the signal at that altitude and the MSISE-90 model [*Hedin*, 1991], per equation (1). These VBC values represent the threshold by which an NLC would be clearly detected by the lidar. The distribution of points versus local time in Figure 1b shows that this level varies significantly with local time. This variability is partly the result of sky conditions, system performance, and the part of the season being sampled. However, if we outline the minimum values, we find the local times between 20 and 04 LST to be most capable of observing weak clouds with values as low as 2.0×10^{-11} $m^{-1}sr^{-1}$. The other local times show a marked decrease in sensitivity with only the moderate to strongest clouds being detectable.

3.1. Derived NLC Properties

[17] Considering the measurement constraints and observations discussed in the previous section, the ARCLITE system was able, over the past seven years, to detect moderate to weak NLCs, primarily during the July–August time frame and for local solar times from 20 through midnight to 04 LST. To study these cloud detections in more detail, we have developed analysis code that determines the cloud height, full-width-half-maximum (FWHM), and peak VBC for each lidar profile containing an NLC. Throughout the analysis, we fix the vertical resolution to 384 m and the temporal resolution to 10 min. Our first step in estimating these properties of the cloud is to determine its aerosol VBC, $\beta_\pi^A(\lambda, z)$, in the manner described by *Thayer et al.* [1995]. Once $\beta_\pi^A(\lambda, z)$ is calculated, each NLC profile is fit by a Gaussian function and a second-order polynomial. The fitted coefficients of the Gaussian are then used to provide the estimates of centroid height, FWHM, and peak value (where the peak value is the height of the Gaussian) for each profile.

[18] Figure 2 is an illustration of the fitting results for an NLC detected on 8 August 1996. Three separate times are presented to illustrate three different conditions of detection. The first time is during low background conditions resulting in a very good fit to the data. This represents a large portion of the data, greater than 90%, where the majority of the NLC detections were taken during low background conditions, as illustrated in Figure 1a. The second time corresponds to an infrequent double NLC layer. In this case, the centroid height lies in between the two peaks, but the other parameters are not significantly impacted. The third case is under high background conditions where the height is accurately determined, but the peak value and the FWHM become less certain because of the increased variance associated with the higher background. This constitutes less than 10% of analyzed cloud data.

[19] All cloud detections from 1994 through 2000 have been analyzed in the manner described above. These fitted products will be used in describing the basic properties of an NLC and, from the many hours of observations, provide a statistical view of NLC characteristics at the Sondrestrom, Greenland, location.

3.2. NLC Observations Indicate Presence and Impact of Gravity Waves

[20] It has been recognized on numerous occasions that short-period wave structures are a prominent feature within

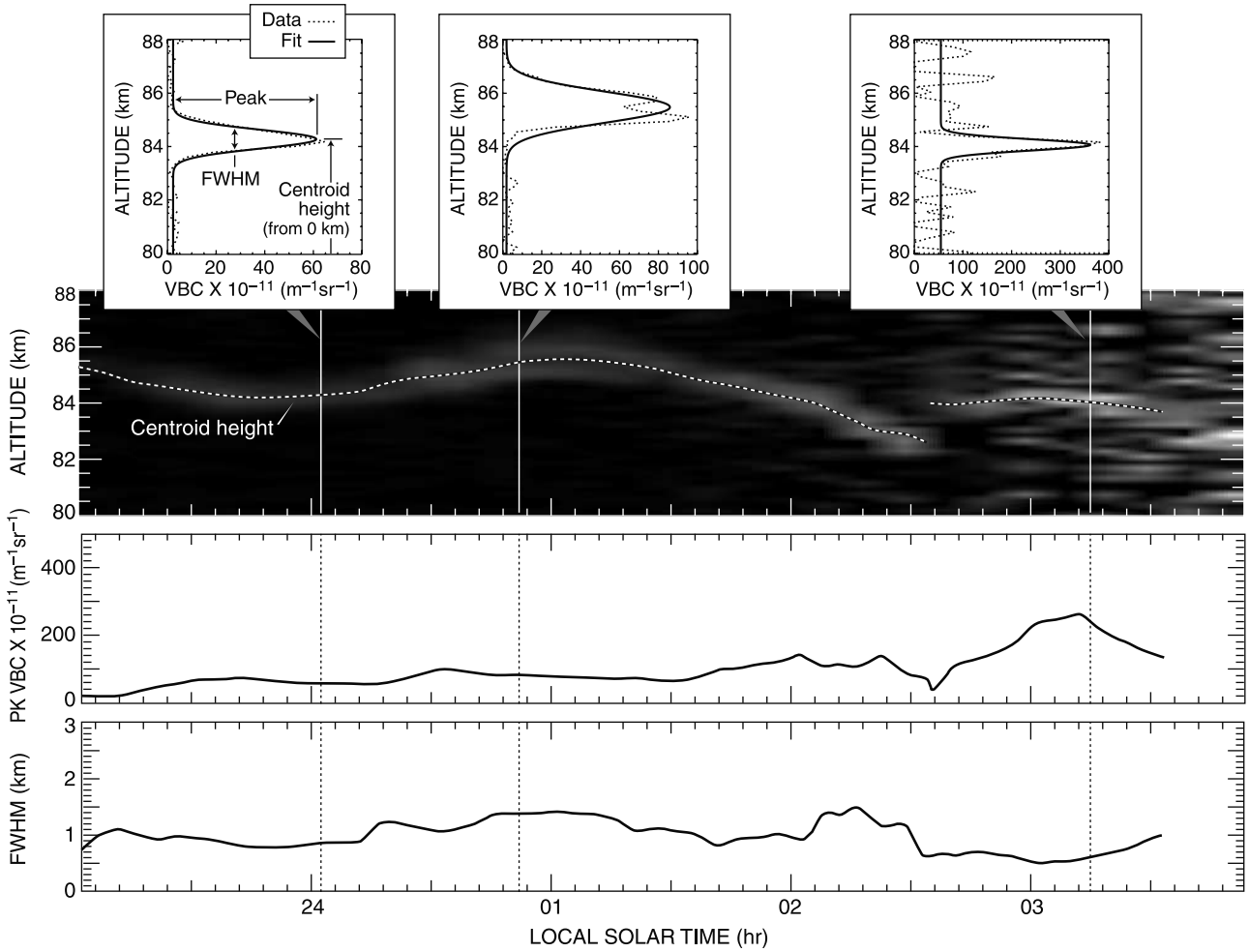

Figure 2. Lidar observations of an NLC on 8 August 1996 and select profiles to illustrate the Gaussian fit procedure to derive the cloud centroid height, FWHM, and VBC.

NLC displays, presumably because of gravity waves [e.g., *Fritts et al.*, 1993]. From a vertically directed lidar beam illuminating an ~10 m spot at NLC altitudes, it would seem reasonable to assume that the presence of wave structures within the NLCs will be transported over the beam by the mean wind enabling a component of the wave structure to be sampled. The variable orientation of the wave vector with respect to the advecting wind field and the speed of the wind field will result in apparent wave structures recorded in the lidar time series.

[21] An illustration of this result is presented in Figure 3, where the centroid heights determined from all clouds detected by the Sondrestrom lidar are displayed versus local solar time. The presence of wave structures is observed in nearly every cloud detected by the lidar over the altitude range from 86 km to about 81 km. Although the time rate of change of these cloud heights is dependent on the vertical winds and the horizontal advection of wave structures, it seems safe to say that short-period (~2 to 3 hour) wave structures, produced by gravity waves, are a ubiquitous feature for the clouds detected over the Sondrestrom lidar site.

[22] Another aspect of gravity-wave presence is its influence on NLC growth and sublimation. *Jensen and Thomas* [1994] introduced gravity-wave perturbations into their two-dimensional numerical model of mesospheric cloud formation. They demonstrated that gravity waves generally act to reduce the brightness, or radius, of the cloud because of the time disparity between the long growth process and the

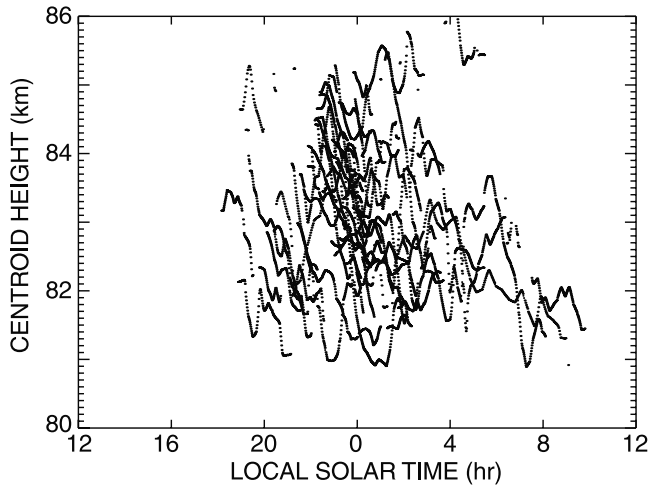

Figure 3. Distribution in local time of derived NLC centroid heights for all cloud detections from 1994–2000.

rapid sublimation process. In the recent modeling effort by *Rapp et al.* [2002], they determined that gravity waves with periods larger than 6.5 hours promote NLC growth while waves with shorter periods lead to NLC sublimation. *Hecht et al.* [1997] reported the first observation of an NLC sublimating due to the passage of a gravity-wave packet using a UV spectrograph and the Sondrestrom Rayleigh lidar. In a paper by *Gerrard et al.* [1998], a collection of Sondrestrom lidar measurements were used to investigate the impact of gravity-wave activity on nightly averaged NLC backscatter strength. The gravity-wave activity was estimated by using the relative density perturbation determined from the lidar signal over the altitude range from 30 to 45 km for observing periods of 2 to 3 hours. A determination of the root mean square (rms) perturbation in relative density was used to indicate gravity-wave activity. A nightly NLC volume backscatter coefficient was determined from the lidar measurements and correlated with the stratospheric estimates of gravity-wave activity. *Gerrard et al.* [1998] analyzed all NLC events from 1994 through 1996 (a total of 17 different nights). The correlation suggested that increasing gravity-wave activity results in an overall decrease in NLC backscatter strength. We have recently updated that study to include most of the cloud events observed after 1996.

[23] The update to Figure 3 of *Gerrard et al.* [1998] is presented in Figure 4. The addition of more events supports the previous years of observation and further solidifies the result presented by *Gerrard et al.* [1998]. Wave periods inferred from the phase progression in the waves were estimated to be of only a few hours for most events. Based on these results, the model by *Rapp et al.* [2002] is consistent with the notion that short-period waves dominate over long-period waves in acting to destroy the NLC.

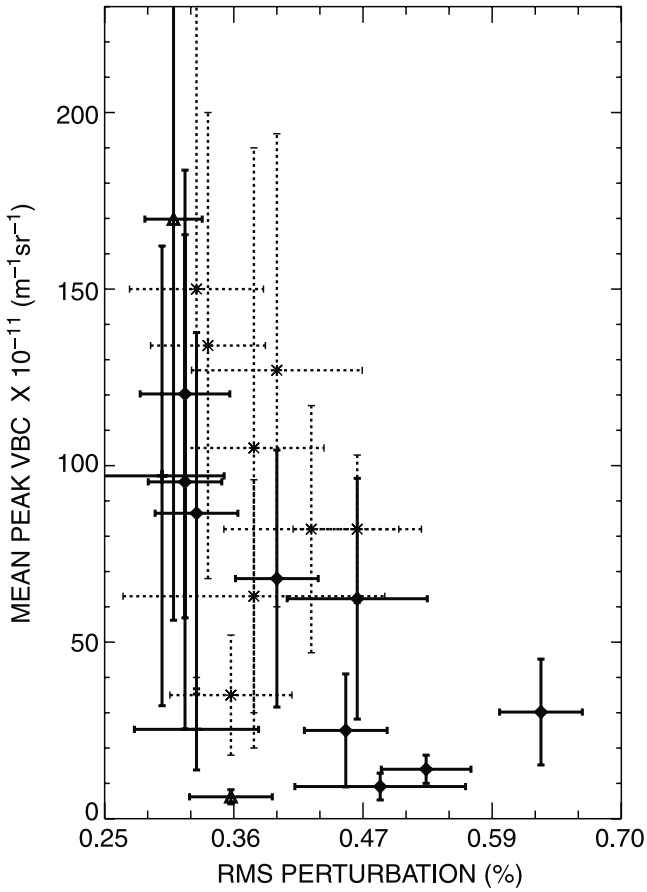

Figure 4. Nightly averaged peak NLC VBC versus derived stratospheric wave activity. The dashed points indicate new data included since *Gerrard et al.* [1998].

3.3. Local Time Behavior in NLC Properties

[24] The basic properties of the observed clouds over 16 hours in local solar time (from 18 to 10 LST) have been determined using the fitting procedure described in Section 3.1. A few caveats about this analysis are required in order to assess properly the results of this section and subsequent sections. First, no distinction has been made regarding data taken in different years and for different months of the NLC summer season. It has been demonstrated, for example by *Gadsden* [1998], that cloud occurrence has increased over the past three decades, with an overlying modulation of about 10 years producing the lowest cloud occurrence about 2 years after the maximum in the solar cycle. *Gadsden* [1998] also indicates that there is no clear change in the basic cloud parameters associated with these long-term changes in cloud occurrence. The seasonal behavior in cloud occurrence has been well documented as having a peak occurrence about three weeks after summer solstice [e.g., *Thomas and Olivero*, 1989]. *Chu et al.* [2001a] have investigated seasonal variations in the cloud parameters from South Pole lidar measurements. They found only the cloud height is affected by day of season; clouds occur at higher altitudes just after solstice and then decrease with height at an estimated rate of 64 m per day. Organizing the Sondrestrom lidar data by day number for all years, we find no such seasonal trend in our centroid heights or in the other parameters.

[25] Considering these caveats, we have organized the cloud properties versus local time irrespective of month or year of the observation. Figure 5 displays the cloud parameters separately, after having been binned into 30-min intervals and averaged, to investigate any local solar time trends. In addition to the three fit parameters, the local time rate of change of the centroid height has been determined for each cloud detected at 10-min intervals. This quantity is effectively the slope of the cloud with time at each cloud point observed in Figure 3. The one-sigma deviation resulting from the averaging is presented for each parameter in each time bin. It should be kept in mind that the number of points going into each 30-min time bin is not the same and follows the distribution shown in Figure 1. Also, the standard deviation basically reveals the geophysical variability in the data as the actual statistical errors in the estimate of these parameters are small.

[26] The mean centroid height within each 30-min LST bin is presented in Figure 5a. Over the core observing period between 20 and 04 LST, the centroid height shows a significant amount of variability. This can also be inferred from the individual centroid heights presented in Figure 3. There does seem to be a preferential decrease in centroid height after 06 LST, but the sample size for this time period is not statitistically significant to draw any firm conclusions. Although there was less coverage in local time, these

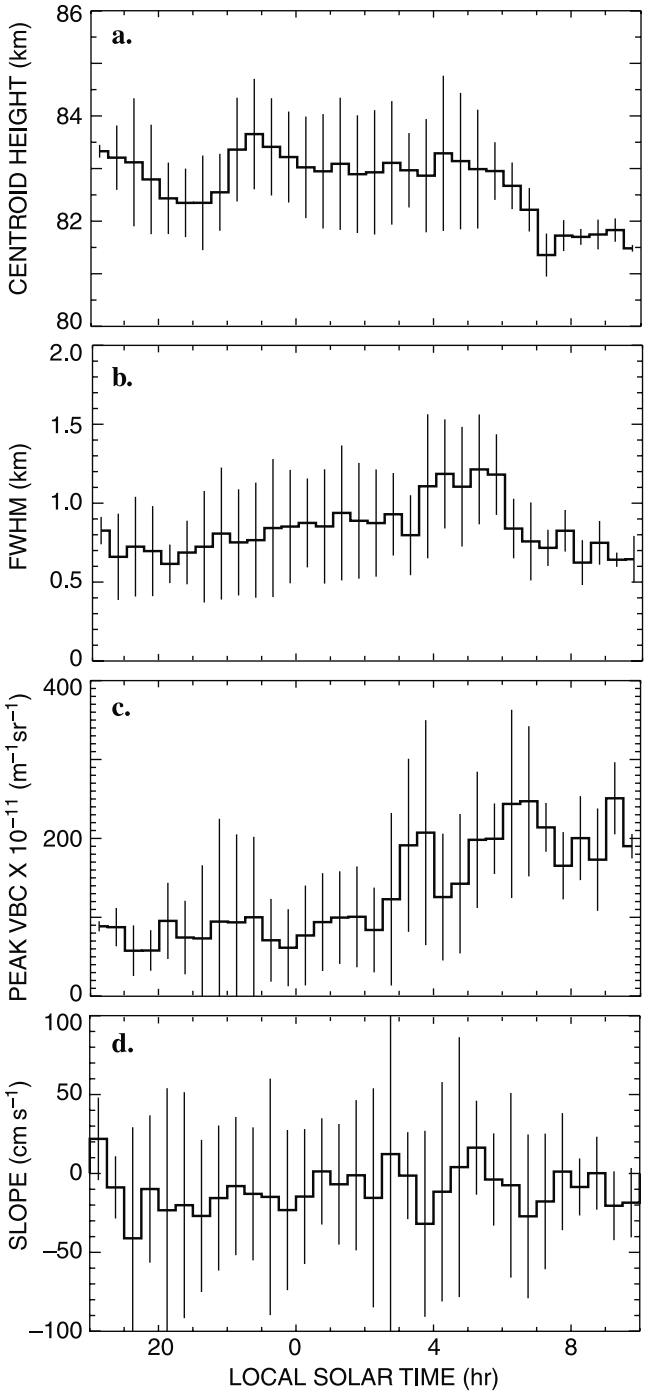

Figure 5. Derived NLC parameters of (a) centroid height, (b) FWHM, (c) VBC, and (d) time rate of change in centroid height averaged into 30-min local time bins. The error bars represent the geophysical variability in the data.

observations are quite different from those observed at both ALOMAR and the South Pole, where diurnal and semidiurnal tidal signatures were observed. The strong influence and continuous presence of gravity waves over the site may mask any local time coherence attributed to tidal influences.

[27] The mean FWHM average values versus LST in Figure 5b show little dependence with local time. The mean FWHM values are often less than 1.0 km. These widths are significantly less than those reported from the South Pole station by *Chu et al.* [2001a]. In their work, they quote RMS values near 0.7 km. For a Gaussian distribution, the FWHM value is the product of the RMS value times the factor $2\sqrt{-2\ln(0.5)}$, which is 2.35482, producing South Pole FWHM values of 1.65 km. Thus our estimates are a factor of two smaller than their measurements. The ALOMAR lidar group has not published its NLC widths, but they also appear to be broader than our results (G. von Cossart, private communication, 1998).

[28] The mean VBC in Figure 5c versus LST does indicate some dependence with LST as the weakest values are observed near midnight and stronger clouds are observed to increase steadily as we move away from midnight (particularly toward the morning hours). This apparent local time dependence in VBC must be countered by whether the lidar was sensitive enough during these times to detect weaker clouds. If we refer back to Figure 1b, we see that for local times earlier than 20 LST and later than 04 LST, the lidar was markedly less sensitive in detecting clouds less than 50-100 $\times$ 10^{-11} $m^{-1}sr^{-1}$ because of the increase in solar background for these times. Thus local time behavior, particularly in backscatter strength, must be carefully scrutinized and, in this case, is related to system sensitivity. Interestingly, the observations by *von Zahn et al.* [1998] show their weakest clouds to occur near midday; thus the benefit of the double etalon receiver in their system certainly improves their lidar performance with local time.

[29] The time series of the lidar NLC observations in Figure 3 enables the assessment of the local time rate of change in the NLC centroid height. The mean time rate of change of the cloud height versus local solar time is presented in Figure 5d. Some explanation is required to interpret this parameter properly. A three-point numerical derivative is performed on each value of cloud centroid height. This represents the slope of the line tangent to the cloud point, and thus the time rate of change of the centroid height in a 10-min interval at 384-m resolution. These slope values have then been organized into 30-min local time bins and averaged to arrive at the plot in Figure 5d.

[30] A number of factors may be involved to produce the observed time rate of change in cloud height, or slope: Its behavior is described by the continuity equation as it pertains to the change in cloud centroid height z_c with time,

$$\frac{\partial z_c}{\partial t} = -\vec{U} \bullet \nabla z_c - z_c \nabla \bullet \vec{U} + P(r, e_i, T), \qquad (3)$$

where the subscript z_c refers to the centroid height of the cloud, the three-dimensional wind vector is given by the symbol U, and $P(r, e_i, T)$ represents cloud growth and sublimation with a dependence on particle radii r, saturation vapor pressure over ice e_i, and temperature T, respectively. The processes involved include advection of structure present in the cloud, shown by the first term on the right-hand side (RHS) of the equation, wind divergence, shown by the second term on the RHS, and the microphysics of cloud growth and sublimation, given by the third term on the RHS. All these factors may contribute to the cloud height change with time, although horizontal advection of tilted structures , vertical motion because of mean updrafts, gravity waves, tides, and particle sedimentation are most

likely the primary contributors, as the timescale for cloud growth microphysics is much longer than that of transport. Assuming this, the expression becomes

$$\frac{\partial z_c}{\partial t} = -w - \vec{U}_h \bullet \nabla_h z_c, \tag{4}$$

where w is the cloud vertical motion resulting from sedimentation and vertical winds, and the second term is the horizontal advection of tilted cloud structures. Although a reasonable amount of variance exists in Figure 5d, it is apparent that there is a mean descent of the clouds for most local times with values reaching in excess of 20 cm/s. The one term that is always downward is the sedimentation rate while downward vertical motion because of gravity waves and tides will depend on their phase.

3.4. Ensemble Behavior in NLC Properties

[31] The strong and assumed random influences of gravity waves on the NLC properties lends itself to an analysis where the cloud properties are collected irrespective of local time. The collective behavior of this ensemble should help reduce the gravity-wave signatures and reveal more basic behavior in the cloud properties, albeit in a gravity-wave dominated environment. Figure 6 presents these results as histograms for the cloud height, FWHM, VBC, and cloud slope. Because the observational makeup of the data set is nearly uniformally distributed around midnight (see Figure 1), a subset histogram for these properties prior to midnight has been included to see if there are any dependencies on premidnight and postmidnight observations.

[32] Figure 6a is the centroid height histogram binned at intervals of 0.5 km altitude. The histogram shows an asymmetric distribution whose most probable value or mode lies within the 82 and 82.5 km bin, as is commonly identified as the typical height of noctilucent clouds. Because of the asymmetry in the distribution, the mean is of higher value, but the mode is the more appropriate value to present. The centroid height distribution is also skewed toward more clouds occurring above 82 km than below. The sharp shelf below 82 km is most likely the result of clouds often sublimating rapidly as they descend along the positive temperature gradient. This rather sharp shelf probably indicates where the saturation ratio equals unity. This lower boundary is controlled by the temperature and, if temperatures varied significantly at these lower altitudes, the distribution in NLC heights would be much less sharp. This seems to provide some indirect evidence of the seasonal invariance in temperature observed by *Lübken* [1999] for altitudes near 82 km. Note, however, that a reanalysis of the rocket data has revealed a great deal more variability and structure in the mesospheric temperature than previously reported [*Rapp et al.*, 2002]. The dashed histogram illustrating clouds prior to midnight shows a slightly higher altitude and a more symmetric distribution.

[33] The FWHM histogram, binned by intervals of 0.1 km, presented in Figure 6b illustrates the most probable cloud width to lie within the 0.6 km and 0.7 km bin. Few clouds are observed to have widths greater than 2.0 km while only a few clouds are observed near our integrated vertical resolution of 0.384 km. The subset of data prior to midnight show no change in the shape of the distribution.

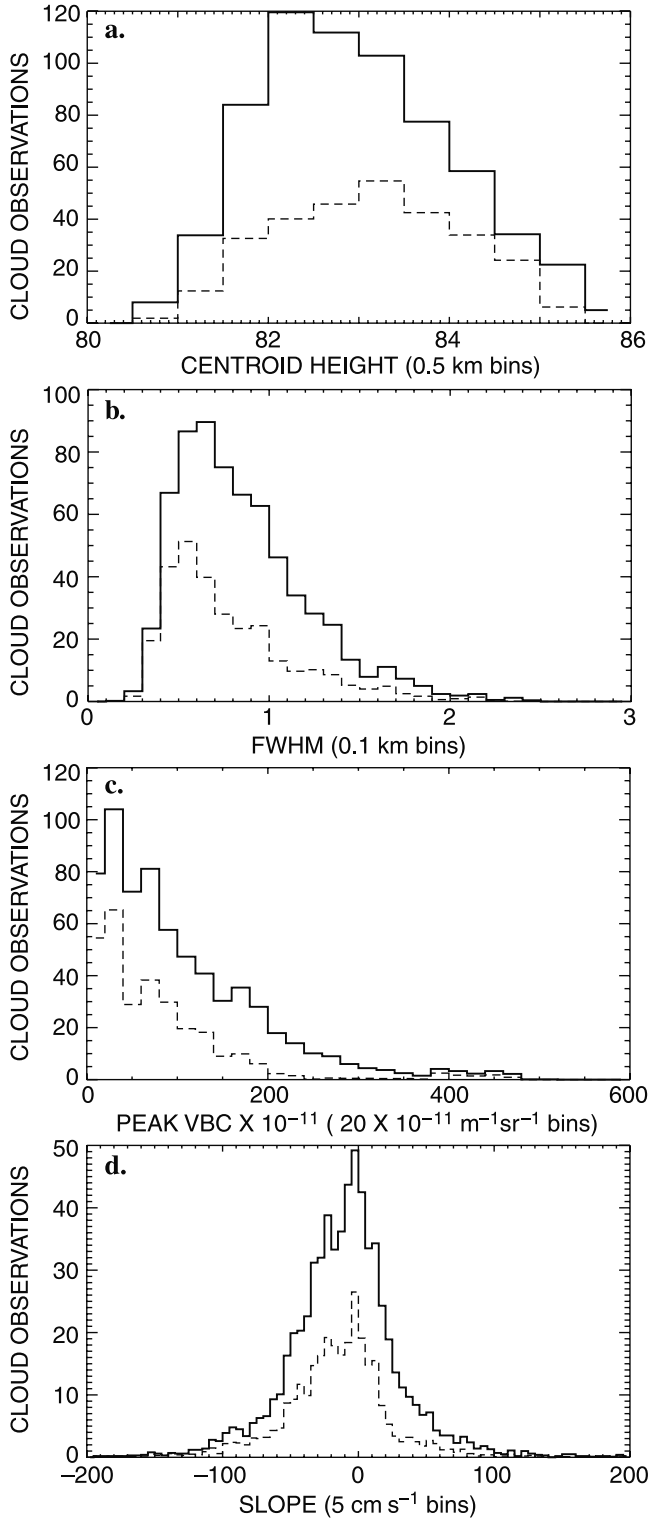

Figure 6. Histograms, irrespective of local time, month or season, of (a) centroid height in 0.5 km altitude bins, (b) FWHM in 0.1 km bins, (c) VBC in 20 $\times$ 10^{-11} m^{-1}sr^{-1} bins, and (d) time rate of change in centroid height in 5 cm/s bins. The dashed line represents the histogram of each value for local times before midnight.

As mentioned previously, this width is smaller than that observed at ALOMAR. Even after integrating the data for one hour, such as performed by *von Zahn et al.* [1998], the widths continue to be smaller by 30 to 40%. Moreover, the South Pole observations determined cloud FWHMs that were over twice as wide as what we observe in Figure 6b (X. Chu, private communication, 2001). This disparity in cloud thickness seems to be the result of short period gravity waves, as will be demonstrated in the section that follows.

[34] The histogram for the peak VBC, collected at intervals of 20×10^{-11} $m^{-1}sr^{-1}$, shows a distribution in Figure 6c that maximizes at a value between 20 and 40×10^{-11} $m^{-1}sr^{-1}$. The number of clouds with strengths greater than this value steadily decreases with a few rare clouds peaking above 400×10^{-11} $m^{-1}sr^{-1}$. Values below 20×10^{-11} $m^{-1}sr^{-1}$ are most likely limited by the variable sensitivity of the lidar system with local time and should not be considered a physical limit to cloud formation.

[35] The histogram for the time rate of change in cloud centroid height, or slope, in intervals of 5 cm/s is presented in Figure 6d. Seldom do the rate magnitudes exceed 100 cm/s, but it is more often observed that the clouds are descending rather than ascending. No change in the distribution is observed for times prior to local midnight, as shown by the dashed line in Figure 6d.

4. Discussion

[36] There appears to be a predominance of gravity-wave influences on the NLC parameters determined from the Sondrestrom, Greenland, lidar observations. This differs from results presented by *von Zahn et al.* [1998] at ALOMAR, as well as recent results by *Chu et al.* [2001b] from the South Pole, where diurnal and semidiurnal tide-like behavior was interpreted after organizing their data versus local time. The ALOMAR observatory near Andoya, Norway (69N,16E), is near in latitude to the Greenland site but is separated in longitude by about 66 degrees. Sondrestrom, Greenland, is inland from the western coast by about 150 km while the ALOMAR site is a coastal site. The South Pole site is, of course, at the highest southern latitude and may experience polar mesospheric conditions quite different from those in the northern hemisphere and at lower latitudes.

[37] The ALOMAR data of *von Zahn et al.* [1998] found a strong anticorrelation in centroid height versus backscatter strength. The South Pole results of *Chu et al.* [2001b] also found a diurnal and semidiurnal oscillation present in the data, but the changes in centroid height and peak backscatter values were well correlated with time. In Figure 7a, each value for the peak VBC and its corresponding centroid height are organized into 0.5 km height bins. The resulting behavior shows that the clouds of strongest backscatter occur at lower altitudes while weaker clouds tend to occur at higher altitudes. This behavior is in agreement with *von Zahn et al.* [1998] and seems to indicate that the largest particles are at the lowest altitudes. This condition would suggest a growth-sedimentation scenario.

[38] The FWHM and its corresponding altitude have also been organized into 0.5 km bins in Figure 7b. Here the clouds display a trend of being thicker at high altitudes while decreasing in thickness with decreasing height. Thus

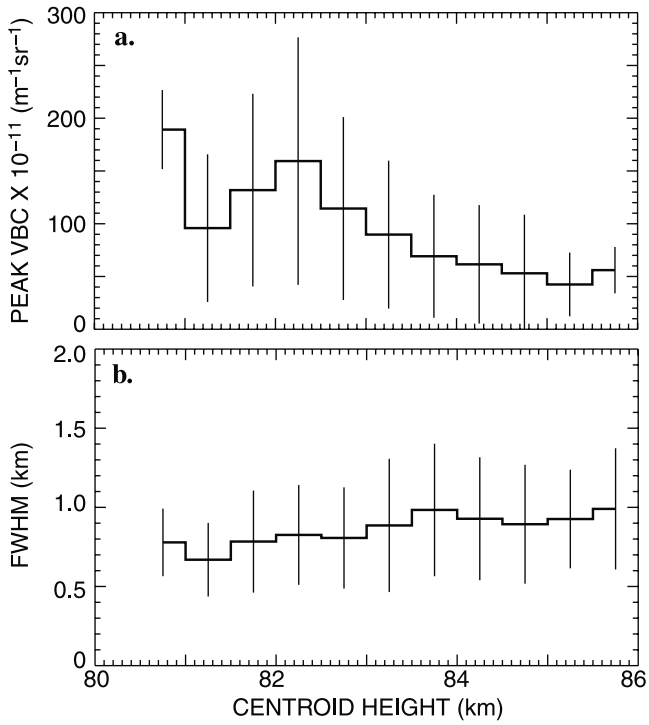

Figure 7. (a) VBC and (b) FWHM values organized into 0.5 km centroid height bins and averaged. The vertical lines represent the standard deviation resulting from the averaging.

clouds at higher altitudes have weaker backscatter, with presumably slightly smaller particle radii, but are broader, while clouds at lower altitudes have stronger backscatter, with slightly larger particles, but are narrower. *Chu et al.* [2001a, 2001b] have reported the cloud heights over the South Pole were discernibly higher (about 2 to 4 km) than that observed in the northern polar regions. If the relationship observed in Figure 7b holds, the difference in cloud thickness between our observations and the South Pole may be caused by this difference in cloud height. However, ALOMAR NLC observations have similar altitude distributions as our observations, and thus the FWHM difference between Sondrestrom and ALOMAR cannot be reconciled in the same manner. However, if gravity waves are influential in determining the cloud's FWHM, the difference in wave behavior between Sondrestrom and ALOMAR might be the cause.

[39] As shown in Figure 6d, the change in cloud height with time seldom exceeds 100 cm/s. This may be due to any combination of particle sedimentation, vertical winds, and horizontal advection of tilted structures. The sedimentation will always be downward producing a negative slope, and careful inspection of Figure 6d reveals a skewness in the distribution toward more negative slopes than positive slopes. This seems reasonable as upward vertical winds producing positive slopes must work against the gravitational descent of the particle, making for smaller overall positive slope values. Another factor is that over the altitude range of detected clouds, from 86 km to 81 km, the fall rate of a particle experiences over a factor of two reduction in speed with descent because of the near scale height increase

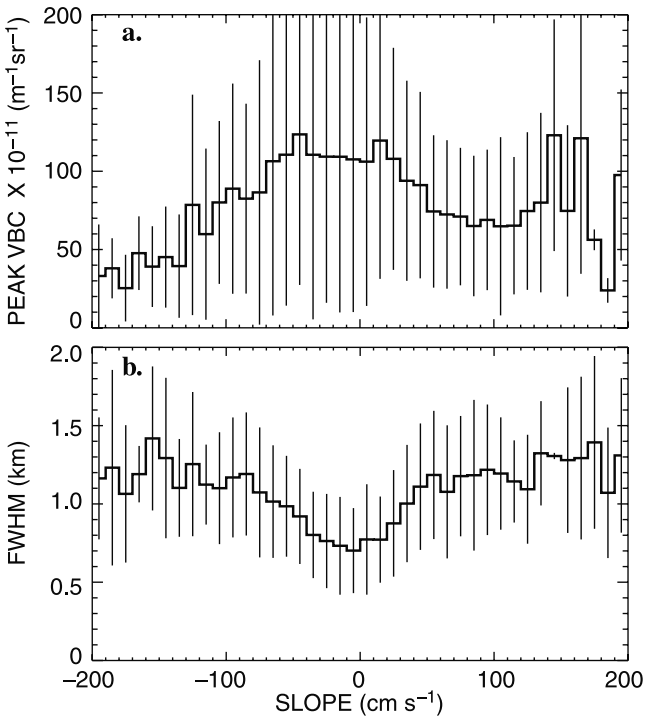

Figure 8. (a) VBC and (b) FWHM values organized into 5 cm/s bins corresponding to the local rate of change in cloud height and averaged. The vertical lines represent the standard deviation resulting from the average.

in atmospheric density. We have determined in Figure 7 that the weaker but thicker NLCs occur at higher altitudes, while stronger but thinner NLCs occur at lower altitudes, and question whether the cloud slopes correlate with this behavior.

[40] The peak VBC and its corresponding local rate of change in cloud height, or slope, are organized into a histogram at 5 cm/s intervals in Figure 8a. Here the histogram illustrates that the strongest backscatter corresponds to the slowest rate of change in cloud height. This supports the results shown in Figure 7, where the strongest backscatter occurred at the lower altitudes where the atmospheric drag is greater, thus slowing the particle descent. The FWHM and its corresponding local rate of change in cloud height are presented in Figure 8b. Again, this supports the results of Figure 7 where the thinner clouds occur at lower altitudes and thus have slower rates of change in cloud height than at higher altitudes. Hence, although a significant amount of scatter is present, it seems that the stronger but thinner clouds at lower altitudes are associated with slow changes in cloud height, and the weaker but thicker clouds at higher altitudes are associated with more rapid changes in cloud height. This result suggests a greater mobility of the NLC particles at higher altitudes, most likely due to the scale height reduction in background density.

[41] It is tempting to apply a growth sedimentation model to describe the observed behavior in Figures 6, 7, and 8, however, the data organization is quite different from a model simulation of microphysical processes leading to the formation of an NLC. As mentioned previously, the lidar is predisposed to observe clouds whose radii are in excess of 20 nm. Therefore, the lidar samples only the larger cloud radii within the total particle size distribution. Once of appropriate size, the cloud may be detectable by the lidar, although it may have gone through a series of growth and sublimation processes before or during the actual detection. To the lidar measurement, the path to achieve the appropriate size for detection is of little consequence, but this path is of large significance to the microphysical modeling efforts, as exemplified by the different approaches used by *Klostermeyer* [1998] and *Rapp et al.* [2002]. However, microphysical models coupled with macroscopic dynamics, such as tides and gravity waves, can provide the physical insight into how the cloud properties are altered by large-scale dynamics.

[42] Therefore, we have performed a numerical experiment with the CARMA model [*Rapp et al.*, 2002], to illustrate the influence short-period gravity waves, such as those observed over Sondrestrom, can have on the cloud microphysics. Two 24-hour runs of the CARMA model were made with each minute of each run sampled for calculations of the model-generated NLC volume backscatter coefficient. Guided by the results in Figure 1, modeled clouds with VBCs greater than 2.0×10^{-11} $m^{-1}sr^{-1}$ at 532 nm were collected. The first run included background conditions of the mesopause region with no wave activity, while the second run included wave activity whose characteristics were similar to those empirically derived by Sondrestrom lidar summer observations [*Gerrard et al.*, 1998]. These types of model runs have been discussed in detail by *Rapp et al.* [2002]. The wave characteristics for the second run were a vertical wavelength of 10 km, a period of 150 min, and a horizontal wavelength of 300 km.

[43] Figure 9 illustrates histograms of centroid height, FWHM, and peak VBC for the two model runs, organized in the same manner as the lidar results presented in Figure 6. Contrasting the two runs and comparing them with the lidar data in Figure 6, we find the model does a better job of reproducing the observed cloud parameter distributions once gravity waves are included in the simulation. The modeled centroid heights without wave activity have a rather restricted range of possible heights while, with the inclusion of gravity waves in the model, the centroid height distribution is rather broad, similar to that observed in Figure 6a. This is largely caused in the model by the up and down transport of the entire cloud by the short-period gravity wave. The modeled FWHM with gravity-wave activity is remarkably similar to the observations presented in Figure 6b. It seems the influence of these short-period gravity waves act to produce thinner clouds than without wave activity by enabling growth in a more restricted altitude region. This may help answer why Sondrestrom observations of FWHM are so much thinner than at the other two lidar sites. The modeled peak VBCs show a shift in their distribution to smaller values when gravity waves are included. This was shown to happen in the model by *Rapp et al.* [2002] when waves of periods shorter than about 6.5 hours were introduced resulting in cloud sublimation. The physical cause is that the cold phase of the 150-min wave is too short for particle growth, but the warm phase is sufficient to affect particle size, eventually leading to the destruction of the cloud. The modeled VBC distribution

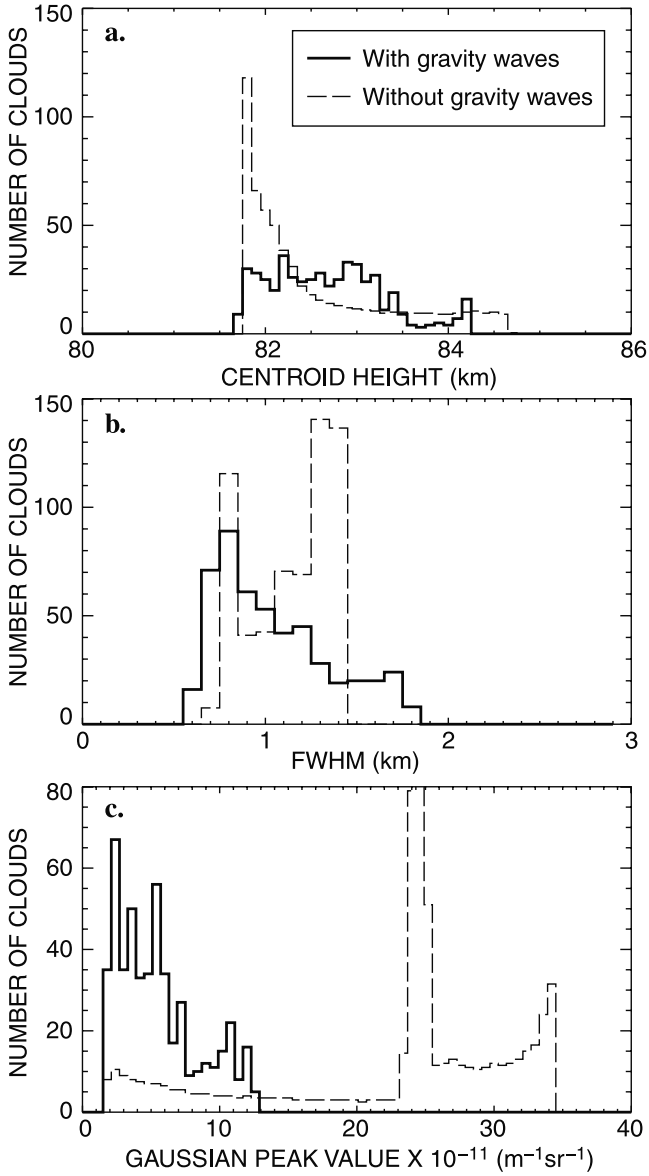

Figure 9. Histograms of (a) centroid height, (b) FWHM, and (c) Gaussian peak value, obtained from two 24-hour CARMA model simulations. Solid lines indicate results from a model run under quiet background conditions (no gravity-wave activity) whereas dashed lines indicate results from a run with gravity-wave activity included (see text for details).

with gravity waves is similar to the observed VBC distribution and supports the results presented in Figure 4. The absolute values of the VBC values are less in agreement with the model, about a factor of ten smaller than the observations.

5. Conclusion

[44] Seven summer seasons of Rayleigh lidar observations from the ARCLITE facility in Sondrestrom, Greenland (67.0N,50.9W), have been compiled to investigate noctilucent cloud behavior as determined from vertically directed lidar backscatter observations. Of the more than 900 hours of lidar observations from 1994 through 2000 covering the time period from late June through August, 220 hours of lidar observations detected enhanced backscatter for altitudes between 81 km and 86 km due to the presence of NLCs. The lidar observations of NLCs covered 16 hours in local time (18 to 10 LST) with further ranges in local time limited by the performance of the lidar system. The percent occurrence of an NLC detection within the 16 hours of local time was about 20%. The ensemble of data, collected irrespective of local time, show the most common centroid altitude or mode occurs between 82 and 82.5 km, but with a distribution sharply skewed, with no detections below about 81 km, and with a broad distribution up to 86 km. The sharp lower boundary in cloud height may result from the strong temperature control over cloud formation and the temperature invariance at this lower boundary. The VBC is most commonly detected near 20.0×10^{-11} $m^{-1}sr^{-1}$, with the occurrence steadily decreasing with larger backscatter strength. NLCs with VBCs lower than 20.0×10^{-11} $m^{-1}sr^{-1}$ were also detected, but a limiting system sensitivity of about 2.0×10^{-11} $m^{-1}sr^{-1}$ prevented detections below that level. The FWHM values lie between 0.6 and 0.7 km, noticeably thinner than those observed at ALOMAR by 30 to 40% and the South Pole by 50% and greater. Estimation of the local time rate of change of NLC height, or slope, shows the clouds seldom exceeding 100 cm/s.

[45] Organizing the NLC parameters of FWHM and VBC versus altitude reveals cloud behavior at high altitudes, near 85 km, of relatively thick clouds (mean FWHM $\sim$1 km) with weaker peak backscatter (mean VBC $\sim 50 \times 10^{-11}$ $m^{-1}sr^{-1}$), while near 82 km the clouds become thinner (mean FWHM values $\sim$0.8 km) and increase in peak backscatter (mean VBC $\sim 150 \times 10^{-11}$ $m^{-1}sr^{-1}$). Upon organizing these parameters versus slope, we found the thicker but weaker clouds observed at higher altitude are associated with relatively steep slopes, while the thinner but stronger clouds occurring at lower altitude are associated with more shallow slopes. As the vertical movement of the cloud particles is altitude dependent because of the nearly factor of three decrease in atmospheric density with height, it would seem appropriate that the higher clouds have greater slopes than the lower clouds.

[46] The local time behavior in cloud properties is less conclusive because of variable system performance outside the core observing time of 20 to 04 LST. Yet gravity waves seem to be a persistent influence on all Greenland lidar detections of NLCs, while tidal influences were prominent in the ALOMAR [*von Zahn et al.*, 1988] and South Pole [*Chu et al.*, 2001b] lidar observations. The random nature of gravity waves may destroy any local time coherence in the cloud behavior. An analysis of stratospheric wave activity and NLC backscatter strength over the entire data set illustrates that strong stratospheric wave activity seems to be correlated with weak NLC backscatter, while weak stratospheric wave activity relates to strong NLC backscatter. This result supports the work of *Gerrard et al.* [1998], who used a subset of the present data set to reveal such a correlation.

[47] The presence of gravity waves will act to perturb the basic state of the mesopause region and consequently affect the microphysics responsible in forming the cloud. The

lidar-derived characteristics of these clouds represent the outcome of this influence. To help understand these observations in a gravity-wave dominated environment, we employed the CARMA model [*Rapp et al.*, 2002] that includes mesospheric cloud microphysics and macroscopic dynamics. The model performed a 24-hour run with no wave activity and a second 24-hour run with short-period gravity-wave activity representative of conditions observed over Sondrestrom in the summer. The model run that included short-period gravity-wave activity reproduced the behavior observed in the ensemble cloud properties by producing a broader altitude distribution, weaker backscatter strength, and thinner clouds. Thus the model results support the observed correlation of wave activity with backscatter strength, and illustrated that thinner clouds occur in the presence of gravity waves, which could explain our observational differences in cloud thickness between Sondrestrom and the other two sites.

[48] **Acknowledgments.** JPT was supported by the NSF Cooperative Agreement ATM-9813556. AJG and TJK were supported in part by NSF Coupling of Energetics and Dynamics of Atmospheric Regions (CEDAR) program grant ATM 98-13828. We would like to thank G.E. Thomas for helpful comments and discussions. We also would like to thank the Sondrestrom site crew and students who have participated over the years in summer lidar measurements at Sondrestrom, specifically, Jo Geddes and Keith Soldavin, Penn State University, and Aimee Merkel, University of Colorado.

References

Charlson, R. J., Noctilucent clouds: A steady-state model, *Q. J. R. Meteorol. Soc.*, *91*, 517–523, 1965.

Chu, X., C. S. Gardner, and G. Papen, Lidar observations of polar mesospheric clouds at South Pole: Seasonal variations, *Geophys. Res. Lett.*, *28*(7), 1203–1206, 2001a.

Chu, X., C. S. Gardner, and G. Papen, Lidar observations of polar mesospheric clouds at South Pole: Diurnal variations, *Geophys. Res. Lett.*, *28*(10), 1937–1940, 2001b.

Fritts, D. C., J. R. Isler, G. E. Thomas, and O. Andreassen, Wave breaking signatures in noctilucent clouds, *Geophys. Res. Lett.*, *20*, 2039–2042, 1993.

Gadsden, M., The north-west Europe data on noctilucent clouds: A survey, *J. Atmos. Sol. Terr. Phys.*, *60*, 1163–1174, 1998.

Gerrard, A. J., T. J. Kane, and J. P. Thayer, Noctilucent clouds and wave dynamics: Observations at Sondrestrom, Greenland, *Geophys. Res. Lett.*, *25*(15), 2817–2820, 1998.

Hansen, G., M. Serwazi, and U. von Zahn, First detection of a noctilucent cloud by lidar, *Geophys. Res. Lett.*, *16*(12), 1445–1448, 1989.

Hecht, J. H., J. P. Thayer, D. J. Gutierrez, and D. L. McKenzie, Multi-instrument zenith observations of noctilucent clouds over Greenland on July 30/31, 1995, *J. Geophys. Res.*, *102*(D2), 1959–1970, 1997.

Hedin, A. E., Extension of the MSIS thermosphere model into the middle and lower atmosphere, *J. Geophys. Res.*, *96*(A2), 1159–1172, 1991.

Hervig, M., R. E. Thompson, M. McHugh, L. L. Gordley, J. M. Russell III, and M. E. Summers, First confirmation that water ice is the primary component of polar mesospheric clouds, *Geophys. Res. Lett.*, *28*(6), 971–974, 2001.

Hesstvedt, E., Note on the nature of noctilucent clouds, *J. Geophys. Res.*, *66*, 1985–1987, 1961.

Hesstvedt, E., On the possibility of ice cloud formation at the mesopause, *Tellus*, *14*, 290–296, 1962.

Jensen, E. J., and G. E. Thomas, A growth-sedimentation model of polar mesospheric clouds: Comparison with SME measurements, *J. Geophys. Res.*, *93*(D3), 2461–2473, 1988.

Jensen, E. J., and G. E. Thomas, Numerical simulation of the effects of gravity waves on noctilucent clouds, *J. Geophys. Res.*, *99*(D2), 3421–3430, 1994.

Jensen, E. J., G. E. Thomas, and O. B. Toon, On the diurnal variation of noctilucent clouds, *J. Geophys. Res.*, *94*(D12), 14,693–14,702, 1989.

Klostermeyer, J., A simple model of the ice particle size distribution in noctilucent clouds, *J. Geophys. Res.*, *103*(D22), 28,743–28,752, 1998.

Klostermeyer, J., Effect of tidal variability on the mean diurnal variation of noctilucent clouds, *J. Geophys. Res.*, *106*(D9), 9749–9755, 2001.

Lübken, F.-J., Thermal structure of the Arctic summer mesosphere, *J. Geophys. Res.*, *104*(D8), 9135–9149, 1999.

Rapp, M., F.-J. Lubken, A. Müllemann, G. E. Thomas, and E. J. Jensen, Small-scale temperature variations in the vicinity of NLC: Experimental and model results, *J. Geophys. Res.*, *107*(D19), 4392, doi:10.1029/2001JD001241, 2002.

Reid, G. C., Ice clouds at the summer polar mesopause, *J. Atmos. Sci.*, *25*, 523–535, 1975.

Thayer, J. P., N. B. Nielsen, and J. Jacobsen, Noctilucent cloud observations over Greenland by a Rayleigh lidar, *Geophys. Res. Lett.*, *22*(21), 2961–2964, 1995.

Thayer, J. P., N. B. Nielsen, R. B. Kerr, and J. Noto, Rayleigh lidar observations during Arctic summer conditions, paper presented at the IGARRS Symposium, Lincoln, Nebr., Inst. of Electr. And Electron. Eng., New York, May 1996.

Thayer, J. P., N. B. Nielsen, R. Warren, C. J. Heinselman, and J. Sohn, Rayleigh lidar system for middle atmosphere research in the Arctic, *Opt. Eng.*, *36*(7), 2045–2061, 1997.

Thomas, G. E., Mesospheric clouds and the physics of the mesopause region, *Rev. Geophys.*, *29*, 553–576, 1991.

Thomas, G. E., and J. J. Olivero, Climatology of polar mesospheric clouds 2. Further analysis of solar mesosphere explorer data, *J. Geophys. Res.*, *94*(D12), 14,673–14,681, 1989.

Turco, R. P., O. B. Toon, R. C. Whitten, R. G. Keesee, and D. Hollenbach, Noctilucent clouds: Simulation studies of their genesis, properties and global influences, *Planet. Space Sci.*, *30*(11), 1147–1181, 1982.

von Cossart, G., J. Fiedler, and U. von Zahn, Size distributions of NLC particles as determined from 3-color observations of NLC by ground-based lidar, *Geophys. Res. Lett.*, *26*(11), 1513–1516, 1999.

von Zahn, U., G. vonCossart, and J. Fiedler, Tidal variations of noctilucent clouds measured at 69 N latitude by ground-based lidar, *Geophys. Res. Lett.*, *25*(9), 1289–1292, 1998.

A. J. Gerrard, College of Agriculture and Technology at Morrisville, State University of New York, Morrisville, New York 13408, USA. (gerraraj@morrisville.edu)

E. Gudmundsson, Sondrestrom Upper Atmospheric Research Facility, Postbox 108, 3910 Kangerlussuaq, Greenland. (eggert@umimmak.srpo.gl)

T. J. Kane, Pennsylvania State University, Electrical Engineering Department, 121 Electrical Engineering East University Park, PA 16802, USA. (tjk7@psu.edu)

M. Rapp, Leibniz Institute for Atmospheric Physics, Schloss-Str. 6, Kühlungsborn D-18225, Germany. (rapp@iap-kborn.de)

J. P. Thayer, SRI International, Center for Geospace Studies, 333 Ravenswood Avenue, Menlo Park, CA 94025, USA. (thayer@sri.com)